

## A GIANT SAMPLE OF GIANT PULSES FROM THE CRAB PULSAR

M. B. MICKALIGER<sup>1</sup>, M. A. McLAUGHLIN<sup>1,2</sup>, D. R. LORIMER<sup>1,2</sup>, G. I. LANGSTON<sup>3</sup>, A. V. BILOUS<sup>4</sup>, V. I. KONDRATIEV<sup>5,6</sup>,  
M. LYUTIKOV<sup>7</sup>, S. M. RANSOM<sup>8</sup>, & N. PALLIYAGURU<sup>1</sup>

*Draft version May 14, 2013*

### ABSTRACT

We observed the Crab pulsar with the 43-m telescope in Green Bank, WV over a timespan of 15 months. In total we obtained 100 hours of data at 1.2 GHz and seven hours at 330 MHz, resulting in a sample of about 95000 giant pulses (GPs). This is the largest sample, to date, of GPs from the Crab pulsar taken with the same telescope and backend and analyzed as one data set. We calculated power-law fits to amplitude distributions for main pulse (MP) and interpulse (IP) GPs, resulting in indices in the range of 2.1–3.1 for MP GPs at 1.2 GHz and in the range of 2.5–3.0 and 2.4–3.1 for MP and IP GPs at 330 MHz. We also correlated the GPs at 1.2 GHz with GPs from the Robert C. Byrd Green Bank Telescope (GBT), which were obtained simultaneously at a higher frequency (8.9 GHz) over a span of 26 hours. In total, 7933 GPs from the 43-m telescope at 1.2 GHz and 39900 GPs from the GBT were recorded during these contemporaneous observations. At 1.2 GHz, 236 (3%) MP GPs and 23 (5%) IP GPs were detected at 8.9 GHz, both with zero chance probability. Another 15 (4%) low-frequency IP GPs were detected within one spin period of high-frequency IP GPs, with a chance probability of 9%. This indicates that the emission processes at high and low radio frequencies are related, despite significant pulse profile shape differences. The 43-m GPs were also correlated with *Fermi*  $\gamma$ -ray photons to see if increased pair production in the magnetosphere is the mechanism responsible for GP emission. A total of 92022 GPs and 393  $\gamma$ -ray photons were used in this correlation analysis. No significant correlations were found between GPs and  $\gamma$ -ray photons. This indicates that increased pair production in the magnetosphere is likely not the dominant cause of GPs. Possible methods of GP production may be increased coherence of synchrotron emission or changes in beaming direction.

*Subject headings:* Crab pulsar, *Fermi*, giant pulses

### 1. INTRODUCTION

The Crab pulsar was discovered by Staelin & Reifenstein in 1968 through its giant pulses. Giant pulses (GPs) can be thousands of times brighter than the average pulse. The temporal occurrence of GPs is random but at frequencies below 3 GHz they always occur at the phase of either the Crab pulsar’s main pulse (MP) or interpulse (IP) (Lundgren 1994). At frequencies from 4 GHz to 8.4 GHz, GPs are emitted at the phases of the MP and IP as well as at the phases of two additional high-frequency components (Moffett & Hankins 1996). Above 8.5 GHz, GPs are again seen at only the phases of the MP and IP (Jessner et al. 2010)

The emission mechanism of GPs is still an open question (e.g. Petrova 2006; Istomin 2004; Weatherall 1998). GPs could be caused by increased pair production in

the magnetosphere, increased coherence of synchrotron emission, or changes in beaming direction. Correlating radio GPs with high-energy photons is one way to determine if increased pair production is a major cause of GPs. A recent model (Lyutikov 2007) proposes that GPs are generated on the last closed magnetic field line near the light cylinder via anomalous cyclotron resonance. If this is true, there would be an increase in  $\gamma$ -rays at the times of radio GPs. Anomalous cyclotron resonances have been previously proposed as a cause of GP emission by Lyutikov et al. (1999) and Machabeli & Usov (1979). We expect the  $\gamma$ -rays to be phase aligned with the radio GPs at 1.2 GHz as the  $\gamma$ -ray and 1.2 GHz radio profiles are aligned (see Figure 1). Since we have such a large data set of GPs, we can correlate them with  $\gamma$ -ray photons to test this model. Correlations between radio GPs and  $\gamma$ -ray photons have been carried out previously by Bilous et al. (2011) and Lundgren et al. (1995). Shearer et al. (2003) correlated radio GPs and optical photons and found a slight correlation, and work by Collins et al. (2012) supports this result.

The *Fermi* Large Area Telescope (LAT) is a pair conversion telescope that operates in the energy range from 20 MeV to 300 GeV. It has a large field of view (2.4 sr), which allows it to rapidly map the entire sky, and very good angular resolution, minimizing background contamination (Atwood et al. 2009). The Crab pulsar is a bright *Fermi* source and has been studied at these energies. Abdo et al. (2010) found that the  $\gamma$ -ray profile is double peaked and matches the 1.4 GHz profile, with the  $\gamma$ -ray peaks leading the radio peaks by  $\sim 0.01$  phase. Since the

<sup>1</sup> Department of Physics, West Virginia University, Morgantown, WV 26506

<sup>2</sup> Also adjunct at the National Radio Astronomy Observatory, Green Bank, WV 24944

<sup>3</sup> National Radio Astronomy Observatory, Green Bank, WV 24944

<sup>4</sup> Department of Astronomy, University of Virginia, PO Box 400325, Charlottesville, VA 22904

<sup>5</sup> Netherlands Institute for Radio Astronomy (ASTRON), Postbus 2, 7990 AA Dwingeloo, The Netherlands

<sup>6</sup> Astro Space Center of the Lebedev Physical Institute, Profsoyuznaya str. 84/32, Moscow 117997, Russia

<sup>7</sup> Department of Physics, Purdue University, 525 Northwestern Avenue, West Lafayette, IN 47907-2036

<sup>8</sup> National Radio Astronomy Observatory, Charlottesville, VA 22903

LAT covers the energies predicted by Lyutikov (2007) and observes the Crab pulsar multiple times per day, we can use *Fermi* data to test Lyutikov’s theory.

The power-law nature of the amplitude distribution of GPs is well known (e.g. Argyle & Gower 1972; Popov & Stappers 2007), but there have been varying values for the power-law index calculated, even for similar frequencies (e.g. Karuppusamy et al. 2010; Bhat et al. 2008). With our large sample of GPs, we can calculate power-law indices over a long timespan. Since the amplitude distribution of pulses from many pulsars is log-normal (Ritchings 1976), GPs must have a different emission mechanism. By comparing our power-law index with those of other neutron star source classes (pulsars, magnetars, RRATs), we may be able to put constraints on the GP emission mechanism.

A  $\gamma$ -ray flare was recently observed from the Crab Nebula by the AGILE satellite (Tavani et al. 2011). The flare lasted from MJDs 55457–55461 and was also observed by *Fermi* (Hays et al. 2010). This occurred during the span of our observations, so we can compare radio and  $\gamma$ -ray properties of the pulsar from before the flare with a few days of data taken about two months after the flare to verify that the flare was not associated with the pulsar. Current theories suggest that the flare was caused by electrons accelerated by magnetic reconnection at the termination shock of the Crab Nebula (e.g. Bednarek & Idec 2011; Bykov et al. 2012; Cerutti et al. 2012).

The plan for the rest of this paper is as follows. Section 2 describes the radio observations and outlines the radio analysis. Section 3 discusses the GP statistics and the power-law index calculations. Section 4 details the correlation between 43-m and GBT GPs. Section 5 presents the *Fermi* data used and its reduction as well as the 43-m/*Fermi* correlation. Section 6 discusses the recent  $\gamma$ -ray flare. Finally, conclusions are offered in Section 7.

## 2. RADIO OBSERVATIONS

We collected data over the course of 15 months using the 43-m telescope (hereafter GB43), located at the National Radio Astronomy Observatory site in Green Bank, WV. The GB43 is funded by MIT Lincoln Labs to perform bistatic radar observations of the ionosphere (Langston 2007). Most of the observations had a center frequency of 1.2 GHz with a useable bandwidth of 400 MHz, with a handful of the later observations centered at 330 MHz, with a useable bandwidth of 150 MHz. All of the observations were taken using 4096 frequency channels and varying sampling times, listed in Table 1. Some of the sampling times used were rather long, and this was done to decrease the data volume. In total, we observed the Crab pulsar for 100 hours at 1.2 GHz and seven hours at 330 MHz. The 330 MHz mode was implemented later and used because pulsars, in general, are stronger at lower frequencies and exhibit a steep spectral index (Lorimer et al. 1995). Even though the smaller bandwidth at 330 MHz reduces sensitivity by almost a factor of 2, the steep spectrum of the Crab pulsar ( $\alpha = 3.1 \pm 0.2$  (Lorimer et al. 1995), where  $S = \nu^{-\alpha}$ ) means that the pulsar is 55 times brighter at 330 MHz than at 1.2 GHz. The flux density from the Crab Nebula is greater at lower frequencies (Cordes et al. 2004) but, due to a shallow power-law index ( $\nu^{-0.27}$ ) (Allen 1973; Bietenholz et al.

1997), at 330 MHz (flux density  $\sim 1288$  Jy) is only 1.4 times brighter than at 1.2 GHz (flux density  $\sim 909$  Jy). Therefore there should be many more GPs above our  $10\sigma$  threshold at 330 MHz than at 1.2 GHz.

Data were taken with WUPPI, the West Virginia University Ultimate Pulsar Processing Instrument. WUPPI is a clone of GUPPI (Green Bank Ultimate Pulsar Processing Instrument) (DuPlain et al. 2008) for use with the GB43. GUPPI is a flexible digital backend for the GBT. Like GUPPI, WUPPI is built from reconfigurable off-the-shelf hardware and software available from the CASPER (Center for Astronomy Signal Processing and Electronics Research) group (Parsons et al. 2009). Both GUPPI and WUPPI sample the data with 8-bit precision over bandwidths as large as 800 MHz, and are capable of recording all four Stokes parameters. To ease disk space usage, only total intensity (Stokes I) was recorded.

The data were processed using a real-time data reduction pipeline on a 16 processor mini-cluster. The pipeline is comprised of a set of scripts, built from freely available analysis software<sup>9</sup>, that can reduce a file in real time. First, a file in PSRFITS format (Hotan et al. 2004) has its mean bandpass divided out. Frequency channels that have intensities above the resulting mean are flagged as containing radio frequency interference (RFI) and removed. Then the resulting file is dedispersed at both a dispersion measure (DM) of zero and the DM of the Crab, which is  $\sim 56.8$  pc cm<sup>-3</sup>; the exact values for each observation, obtained from the Jodrell Bank Crab Pulsar Monthly Ephemeris<sup>10</sup> (Lyne et al. 1993), are listed in Table 1. The DM of the Crab pulsar can vary on a monthly timescale by  $\sim 0.01$  pc cm<sup>-3</sup>. In order to keep processing in real-time we did not correct for this. To ease space requirements, raw data were not kept, so we could also not correct for this later. Errors in GP arrival times due to an incorrect DM on the order of 0.01 pc cm<sup>-3</sup> are  $\sim 20$   $\mu$ s, which is less than the sampling time. Both resulting time series are then searched for single pulses with a peak signal-to-noise (S/N) above  $10\sigma$  using our single pulse search (based on the algorithm described by Cordes & McLaughlin (2003)). Our  $10\sigma$  definition of a GP is somewhat arbitrary because there is no set threshold for a GP as the weakest GPs have yet to be observed. The current population of observed GPs accounts for no less than 50% of the pulsed emission at frequencies around 1.6 GHz, and the inclusion of the weakest GPs could bring that number up to 90% (Majid et al. 2011). A GP time-of-arrival (TOA) (measured by taking the arrival time of the peak of the pulse), the S/N of that peak, and the pulse width, taken as the width of a best-fit top hat function, are recorded for each pulse. The TOAs from each time series are compared and if a pulse detected at the DM of the Crab is within 0.1 s of a zero DM pulse, the S/N is checked for both pulses<sup>11</sup>. If the S/N is higher in the zero DM pulse, the pulse is assumed to be due to RFI and removed. The pipeline outputs a profile for each GP and produces an average folded profile for the entire observation, a plot of GP arrival

<sup>9</sup> <http://sigproc.sourceforge.net>

<sup>10</sup> <http://www.jb.man.ac.uk/~pulsar/crab.html>

<sup>11</sup> This is of the order of the frequency dependent arrival time delay across the band, and is used as it removes very nearly all RFI, while removing few real GPs.

time vs pulse phase, and an average GP profile, made by summing all of the individual GP profiles.

Figure 2 shows the number of GPs detected versus pulse phase. It is worth noting that, although there were only four post-flare observing epochs, there are many more GPs than were recorded in all of the pre-flare data. This was due to a receiver upgrade which resulted in a large increase in sensitivity between our observations on MJD 55412 and MJD 55516. At frequencies below 5 GHz (Cordes et al. 2004), most detected GPs come at the phase of the MP, with the rest at the IP phase. In our data,  $\sim 87\%$  of detected GPs were at the phase of the MP, while the other  $\sim 13\%$  were at the phase of the IP. Only 5% of GPs detected by Cordes et al. (2004) at 1.2 GHz were at the phase of the IP, but Karuppusamy et al. (2010) found that  $\sim 12\%$  of GPs detected at 1.4 GHz were IP GPs. For detected pulses that show up out of phase with the MP and IP, the frequency versus time plots are checked by eye to see if they show the proper quadratic frequency sweep for a DM of  $56.8 \text{ pc cm}^{-3}$ . If they do not, those pulses are removed. In most cases, the RFI removal process mentioned above removes most of these false detections before they are checked by eye. We found no events at phases other than those of the MP or IP that showed the proper frequency sweep to be a real GP.

Most of the GPs we detected have a constant intensity across the entire band. Some of them, however, show variations in amplitude as a function of frequency, which have been seen before (e.g. Karuppusamy et al. 2010). We also see variations in amplitude between days, which is likely due to refractive interstellar scintillation (RISS), which can affect the strength of pulses on a timescale of days.

In order to determine if the time stamps for the GB43 are accurate, a short ( $\sim 10$  min) observation of the Crab pulsar was made contemporaneously on MJD 55406 at similar frequencies with the GB43 and GBT. The GB43 used a center frequency of 330 MHz, while the GBT used 350 MHz. GPs were detected in each data set and their TOAs were compared. As can be seen in Figure 3, the pulse shapes of contemporaneous GPs are similar, and the TOAs, converted to infinite frequency at the solar system barycenter, have identical arrival times to within the instrumental resolution.

Figure 4 shows the average profile of the Crab pulsar at 1.2 GHz and 330 MHz. The intensities are in arbitrary units. The MP and IP are visible at both frequencies. The increased width at low-frequency is due largely to DM smearing, which is on the order of 2.4 ms at the bottom of the band. The 1.2 GHz profile exhibits a weak low-frequency component (LFC), about one-tenth of a pulse phase ahead of the MP (e.g. Moffett & Hankins 1996). At 330 MHz there is a precursor (PR) to the MP (e.g. Rankin et al. 1970) which is broad enough at this frequency that it shows up as the first peak of the double-peaked MP (see Karuppusamy et al. 2012, for the frequency evolution of the PR), which is visible in the low-frequency GBT profile from MJD 55406 (Figure 1). Due to a much larger effective resolution, the MP in the GB43 profile is unresolved and appears to have a single peak. Table 2 lists the effective resolutions at the top and bottom of the band for both the 330 MHz and 1.2 GHz GB43 observations as well as the GBT 350 MHz observation.

The full-widths-at-half-maximum (FWHMs) of the MP and IP from the GB43 profiles are  $\sim 305 \mu\text{s}$  and  $\sim 360 \mu\text{s}$  at 1.2 GHz and  $\sim 3.2$  ms and  $\sim 1.5$  ms at 330 MHz. At 330 MHz, the MP is wider than the IP due to its overlap with the PR (Rankin et al. 1970). The average GP profiles, however, are narrower than the average folded profiles at both frequencies (see Figure 5), with FWHMs of  $\sim 140 \mu\text{s}$  for both the MP and IP at 1.2 GHz, and  $\sim 1.1$  ms at 330 MHz for both the MP and IP. It has been suggested by Popov et al. (2006) that every pulse at the phase of the MP and IP is a GP, and that normal emission only comes from the PR, where no GPs have been seen. We also have not seen any GPs at the phase of the PR at 330 MHz in our data. Even though our observed GP profiles are narrower than the average folded profiles, this hypothesis is not ruled out. Popov & Stappers (2007) found that pulse width is inversely proportional to pulse intensity, so lowering our S/N definition of a GP would include wider GPs which could possibly increase the width of the average GP profile to that of the folded profile. Also, the phases of weaker GPs may have more deviation from the center phase of the MP and IP than stronger GPs, leading to a wider average profile. Unfortunately, we were unable to lower our GP threshold below  $10\sigma$  as this resulted in many spurious pulses.

### 3. AMPLITUDE DISTRIBUTIONS

A total of 93698 GPs were observed with the GB43. At 1.2 GHz we recorded 76707 GPs at the phase of the MP and 10871 GPs at the phase of the IP, and at 330 MHz 5232 MP and 888 IP GPs were recorded. Due to low GP statistics on some days, only 78574 MP GPs and 9693 IP GPs were used in fitting the amplitude distributions.

We calculated, through least-squares fitting, power-law indices for the differential amplitude distributions of MP and IP GPs at both 1.2 GHz and 330 MHz for each day separately. Figure 6 is an example of a power-law fit for the MP. We noted that the power-law index of GPs varied daily, as was previously reported by Lundgren et al. (1995) at similar frequencies. This gave a range of power-law indices from  $2.1 \pm 0.3$  to  $3.1 \pm 0.2$  for MP GPs at 1.2 GHz,  $2.4 \pm 0.4$  to  $2.81 \pm 0.03$  for IP GPs at 1.2 GHz,  $2.5 \pm 0.2$  to  $2.95 \pm 0.09$  for MP GPs at 330 MHz, and  $2.4 \pm 0.2$  to  $3.1 \pm 0.2$  for IP GPs at 330 MHz. Table 3 lists the power-law indices for each day. These indices agree with other published power-law indices, listed in Table 4. The range of indices is likely due to wider GPs having steeper spectra, as was seen by Popov et al. (2008). We did not have the time resolution to separate the GPs by width, as the widest GPs reported by Popov et al. (2008) were  $64 \mu\text{s}$ , which is the shortest sampling time we used.

We were unable to properly calibrate the data due to lack of any off-source pointings and/or observations with a pulsed cal. There were also doubts as to the stability of the receiver over long timespans. We were able to do a rough calibration, however, by correcting for RISS, which affects the strength of all GPs by the same amount, so there should be no change to the power-law slope. Rickett & Lyne (1990) found that the RISS timescale for the Crab pulsar scales as  $\nu^{-2.2}$ . Based on this, the timescales at 1.2 GHz and 330 MHz are 1.7 days and 30 days, respectively. A Lomb-Scargle analysis (Scargle

1982) of the periodicity of GP arrival times yielded periodicities of 0.41 days at 330 MHz and 0.99 days at 1.2 GHz. The  $\sim$ one day periodicity of the GP arrival times in the 1.2 GHz data is on the order of the RISS timescale at that frequency, but the same periodicities were also seen in the randomized data set, so they are not significant. We attempted to correct for RISS by scaling observations based on the brightness of their folded profiles. However, if GPs dominate the average folded profile, as was seen by Popov et al. (2006), any intrinsic variations in their strength will affect this correction. To determine if this was true, we removed the GPs from the average profile. We found that at 1.2 GHz the amplitude of the average profile without GPs was 1% less than the average profile with the GPs, and at 330 MHz was 2% less. We therefore concluded that GPs do not dominate the average profile. One possible reason why our results are the opposite of what was seen by Popov et al. (2006) is that they recorded all GPs above  $5\sigma$ , while we were only able to record GPs above  $10\sigma$ . Therefore, it is possible that weaker GPs dominate the average profile. If the average profile is truly dominated by GPs, then correcting for RISS is complicated, but since we do not see this, we used the following correction.

We took the brightest folded profile from each of our three observing epochs (pre-flare 1.2 GHz, 330 MHz, post-flare 1.2 GHz) and scaled all of the folded profiles from those epochs to that profile. That provided us with a scaling factor for each day, by which we then multiplied the GP S/Ns. We also compared our indices with power-law indices of other source classes in an attempt to constrain the GP emission physics. Other source classes and their indices are listed in Table 5. Although most normal pulsars have log-normal distributions, some pulsars have amplitude distributions that have power-law tails. These power-law exponents are included in Table 5 under ‘Normal Pulsars’. Our power-law indices match those of magnetars and RRATs, but do not match the power-law tails seen from normal pulsars.

Also seen in Figure 6 is a non power-law tail, which is seen on all days in both the MP and IP. This deviation is significant, and was also seen by Cordes et al. (2004), who postulated these outlying GPs could be supergiant pulses, indicating that there may be two distinct mechanisms for GP generation. These supergiant pulses account for slightly less than one percent of the GPs used in the amplitude distributions.

#### 4. CORRELATING RADIO GPS FROM THE GB43 AND GBT

For 16 hours over the span of eight days, we observed the Crab pulsar simultaneously with the GB43 and GBT. The center frequency for GB43 observations was 1.2 GHz with 400 MHz of useable bandwidth, while that of the GBT was 8.9 GHz with 800 MHz of useable bandwidth. At high frequencies the majority of GPs come at the phase of the IP, with fewer MP GPs and few GPs from high-frequency components (HFCs) (see Figure 7 for a comparison of the folded profile at high and low frequencies). For this work, we did not use any HFC GPs in our correlation analysis. We matched the barycentered arrival times of the 39900 GPs with  $S/N > 10$  recorded with the GBT (1035 MP GPs, 38865 IP GPs) with the 7933 GPs recorded simultaneously with the GB43 (7466 MP GPs, 467 IP GPs). We found that 236 low-frequency

MP GPs were also detected simultaneously at 8.9 GHz. These GPs were neither the strongest nor the weakest pulses from either data set. The chance probability of this occurring is zero percent. This is not surprising, as we know that the high- and low-frequency MP are the same component. We did expect, however, that all of the MP GPs detected at 8.9 GHz would be the strongest of the MP GPs detected at 1.2 GHz, since the MP is significantly weaker at 8.9 GHz than at 1.2 GHz. All chance probabilities were calculated assuming Poisson statistics, using the formula  $P = \frac{e^{-\lambda} \times \lambda^K}{K!}$ , where  $\lambda$  is the number of detections expected and  $K$  is the number of detections actually recorded.

Moffett & Hankins (1996) first noticed that the low- and high-frequency IP components of the folded profile are separated by  $10^\circ$ , which is about  $970 \mu\text{s}$ . We checked to see if any low-frequency IP GPs were simultaneously detected at 8.9 GHz. Only 23 were found ( $\sim 5\%$ ), with a zero percent chance occurrence, but this is expected since the spectral index of GPs is steep (Popov et al. 2008). We then checked to see if low- and high-frequency IP GPs commonly occurred within the same rotation period of the pulsar, as was previously seen by Popov et al. (2008). In our data, we found 15 instances ( $\sim 4\%$ ) of low-frequency IP GPs occurring within one spin period of a high-frequency IP GP. The probability of this measurement happening by chance is 9%. In four of these instances the GPs are within one  $\mu\text{s}$  of each other and the chance probability of this occurring is zero. In the other 11 instances, the GPs are almost one spin period apart. These are likely statistical, as there is a 10% chance of this occurring randomly. The fact that only four of the 1.2 GHz IP GPs occur within one  $\mu\text{s}$  of an 8.9 GHz IP GP suggests that the high and low-frequency IP may be created by different physical processes (Moffett 1997) possibly due to emission from different regions in the magnetosphere (Hankins & Eilek 2007). However, since the chance probability of detecting four low- and high-frequency IP GPs within one  $\mu\text{s}$  is zero, it seems likely that the high-frequency IP is related to the low-frequency IP, as seen by Popov et al. (2008) in previous correlations of IP GPs at 600 and 4850 MHz. One possibility is that both the high and low-frequency IP are reflections of the MP off of the magnetosphere (Petrova 2009). In this scenario, radio emission from the MP originating deep in the magnetosphere propagates through the electron–positron plasma that fills the magnetosphere. Transverse scattering causes the MP emission to be backscattered, causing it to arrive at a different pulse phase. If this was the case, we would expect a linear relationship between the strength of the MP and IP in the folded profile for each observation. As shown in Figure 8, we do see such a relationship at both 1.2 GHz and 330 MHz. The slopes for the 1.2 GHz and 330 MHz relations are  $0.310 \pm 0.004$  and  $0.58 \pm 0.08$ , respectively.

#### 5. CORRELATING RADIO GPS FROM THE GB43 WITH $\gamma$ -RAY PHOTONS FROM *FERMI*

One of the predictions of Lyutikov (2007) is that there would be increased  $\gamma$ -ray flux during a GP. In order for this model to accurately reproduce the data, the plasma density of the GP emission region must be  $\sim 10^5$  higher than the minimum Goldreich-Julian density and the duty cycle of the pulsar must be 0.001. This increase in density

could be due to enhanced pair production in the pulsar magnetosphere. If correct, these high-energy particles, produced during reconnection close to the Y point, where the last closed magnetic field lines approach the light cylinder at the magnetic equator (Lyutikov 2007), are expected to produce curvature radiation from 0.1–100 GeV (depending on the value of the Lorentz factor  $\gamma$ ) at the time of a GP. This curvature radiation would cause an increase in  $\gamma$ -rays at the times of radio GPs.

Data were downloaded from the *Fermi* online archive<sup>12</sup> for days when radio observations occurred. ‘Source’ class events from Pass 7 data above 100 MeV were selected in an energy dependent radius ( $\theta < \text{Max}(6.68 - 1.76\log(E), 1.3)^\circ$ , where E is the energy of the photon in MeV) around the position of the pulsar (Abdo et al. 2010). Only photons in Good Time Intervals (GTIs) were selected and those with a zenith angle  $> 100^\circ$  were excluded to discriminate against  $\gamma$ -rays generated in the Earth’s atmosphere. The photons were converted to infinite frequency at the solar system barycenter using the *gtbary* utility from the Fermi Science Tools package.

We then searched for coincidences between radio GPs and  $\gamma$ -ray photons. Due to clock errors in the backend on four days at 1.2 GHz (55097, 55257, 55290, 55346), only 75131 MP and 10771 IP GPs were used. However, all of the 5232 MP and 888 IP GPs recorded at 330 MHz were used. This resulted in a total of 92022 GPs and 393  $\gamma$ -ray photons, with an average  $\gamma$ -ray photon rate of  $\sim 16$  photons/hour, in agreement with the 15 photons/hour seen by Abdo et al. (2010). *Fermi* observes the Crab pulsar for about 11 hours per day, resulting in about 34 hours of simultaneous observing time. We also made energy cuts and searched for coincidences between radio GPs and  $\gamma$ -ray photons above both 500 MeV and 1 GeV.

Based on comparisons with correlations of randomized data, we found no significant correlation between MP or IP GPs at both 1.2 GHz and 330 MHz and  $\gamma$ -ray photons out to a time lag of  $\pm 3 \times 10^6$  spin periods. Since there was not necessarily the same number of randomized  $\gamma$ -ray photons during an observation as there were real  $\gamma$ -ray photons, we used this large time lag to make sure that there were the same number of real and randomized correlations once all of the  $\gamma$ -ray photons were included. The mean and standard deviation of the randomized correlations were calculated by randomly assigning  $\gamma$ -ray photon arrival times within GTIs and correlating them with GP TOAs. Figure 9 shows the results of this correlation analysis. The random correlations are the mean of 10000 trials, and the error bars represent one standard deviation. The largest deviation from the mean is a  $2.4\sigma$  anticorrelation between  $\gamma$ -ray photons and post-flare 1.2 GHz MP GPs at a time lag of 20000 spin periods, while the largest correlation is  $2.1\sigma$  for the pre-flare IP at 1.2 GHz at a time lag of 200000 spin periods. The maximum correlation/anticorrelation for each frequency at each energy cut is shown in Table 6. For both the MP and IP for each of the three data sets (pre-flare 1.2 GHz, 330 MHz, post-flare 1.2 GHz), there are at most two time lags where the correlation exceeds  $2\sigma$ . There are a total of 49 time lags included in the correlation, so two time lags are only four percent of the total data, while we statistically expect five percent of the data to have

correlations beyond  $2\sigma$ . Given the low significance and large time lag of these results, they do not provide any compelling case for a physical origin.

Selecting only  $\gamma$ -ray photons above 500 MeV resulted in a total of 119 photons. The maximum correlation for this more restricted set was  $2.3\sigma$  at a time lag of one spin period for pre-flare MP at 1.2 GHz. The maximum anticorrelation was  $3.5\sigma$  at a time lag of 20000 spin periods for the post-flare MP at 1.2 GHz. No more than one time lag for any data set was had a correlation over  $2\sigma$ , so those measurements above  $2\sigma$  are statistically insignificant. Statistically, only half of a percent of the data should be above  $3\sigma$ , and two percent of our data have a  $3.5\sigma$  significance. However, this is likely due to the coarseness of our time lags. Given more time lags, we would expect this significance to drop below  $3\sigma$ .

Only 65  $\gamma$ -ray photons had energies above 1 GeV. The maximum correlation occurred in the 1.2 GHz pre-flare MP with a  $3.2\sigma$  significance at a time lag of one spin period. The maximum anticorrelation was  $1.2\sigma$ , which occurred in the 1.2 GHz pre-flare IP at a time lag of 200 spin periods. As with the 500 MeV energy cut, we only see at most one time lag with above  $2\sigma$ , which is insignificant. Similarly, the  $3.2\sigma$  significance is likely due to the coarseness of our time lags, and would likely drop given more time lags.

## 6. CRAB NEBULA $\gamma$ -RAY FLARE

The recent  $\gamma$ -ray flare from the Crab Nebula was detected by the AGILE satellite above 100 MeV (Tavani et al. 2011). Elevated  $\gamma$ -ray flux was observed from MJDs 55457–55461. No variations in pulse shape were found at  $\gamma$ -ray (Hays et al. 2010), X-ray (Tavani et al. 2011), or radio (Espinoza et al. 2010) energies. Espinoza et al. (2010) also found no increase in pulsed radio flux, glitches, or changes in DM around the date of the flare. Our closest observations before the flare were on MJD 55412 at 330 MHz and MJD 55352 at 1.2 GHz, and our first observation after the flare was on MJD 55516 at 1.2 GHz.

We looked for changes in the average pulse profile, GP shape, power-law index, and  $\gamma$ -ray correlation in our pre- and post-flare 1.2 GHz data. We found no significant differences in the pulse profile shape and the average GP shape (Figure 10) before and on four days about two months after the flare. The pre-flare MP power-law indices are in the range  $2.1 \pm 0.3$  to  $3.1 \pm 0.2$ , while the post-flare power-law indices for the MP and IP are  $2.56 \pm 0.05$  to  $2.93 \pm 0.05$  and  $2.4 \pm 0.4$  to  $2.81 \pm 0.03$ , respectively. We were unable to calculate power-law indices for the IP pre-flare due to low IP GP statistics. The largest anticorrelation between  $\gamma$ -ray photons and GPs was seen in the post-flare data, but it is still on the order of correlations/anticorrelations seen in pre-flare data, both at 1.2 GHz and 330 MHz.

## 7. CONCLUSIONS

We compared GB43 and GBT GPs and found that 3% of MP GPs and 5% of IP GPs at 1.2 GHz were simultaneously detected at 8.9 GHz. The probability of either of these events occurring by chance is zero. Also, an additional four IP GPs at 1.2 GHz were within one  $\mu$ s of an IP GP at 8.9 GHz, with a zero percent chance probability.

<sup>12</sup> <http://fermi.gsfc.nasa.gov/cgi-bin/ssc/LAT/LATDataQuery.cgi><sup>1</sup>This may suggest that, although the folded profiles are

much different at the two frequencies, the emission mechanism is similar. However, the low percentage of low- and high- frequency IP GPs within one  $\mu\text{s}$  could mean that the IP emission mechanism is different at higher frequencies, especially since the high-frequency IP is shifted by 10 degrees.

Long observations allowed us to collect the largest sample of GPs to date, which we then used to calculate power-law indices for fits to amplitude distributions. These power-law indices agree with previously published values. A comparison of these indices to other source classes shows that GP emission is not exactly related to emission from other source classes and most closely matches the emission from magnetars and RRATs.

We found no significant correlations between GB43 GPs and *Fermi*  $\gamma$ -ray photons in the energy range 0.1–100 GeV. There are only a few correlations/anticorrelations in the MP and IP at both frequencies. They occur at different time lags and are within  $2.5\sigma$  of the mean for a correlation with randomized data. This suggests that although increased pair production in the magnetosphere may contribute to GP occurrence, it is not a dominant factor. More likely possibilities for GP generation are increased coherence or changes in beaming.

Multifrequency correlations have been searched for previously. Shearer et al. (2003) found a 3% increase in the brightness of optical pulses at the time of GPs and Collins et al. (2012) found a slight correlation between GPs and enhanced optical pulses, which supports our  $\sim 2\sigma$  correlations/anticorrelations in suggesting that there are small fluctuations in the magnetospheric particle density during GPs. The anticorrelations, however,

would suggest that increased particle density would lead to more radio emission and less  $\gamma$ -ray emission, which does not make sense in the context of Lyutikov’s theory. Since the significance of the anticorrelations are on the order of the significance of the correlations, we assume that these are insignificant. Lundgren et al. (1995) found that the  $\gamma$ -ray flux does not vary by more than 2.5 times the average flux during a GP. Bilous et al. (2011) ruled out a strong correlation between GPs at 8.9 GHz and  $\gamma$ -ray photons above 100 MeV. They were able to put an upper limit on the  $\gamma$ -ray flux during IP GPs of 8–16 times the average pulsed flux, suggesting that there still might be a slight correlation between GPs and  $\gamma$ -ray photons. We could not carry out the same experiment because we did not have sufficient  $\gamma$ -ray photons to compare the  $\gamma$ -ray profile made with  $\gamma$ -ray photons around GPs with the  $\gamma$ -ray profile excluding  $\gamma$ -ray photons around GPs.

The recent  $\gamma$ -ray flare from the Crab Nebula occurred during the span of our observations, so we were able to compare the behavior of the Crab pulsar before and after the flare. We found no significant changes in pulse shape, power-law index, or  $\gamma$ -ray correlation, suggesting that there was no change in the properties of the pulsar during the flare.

## 8. ACKNOWLEDGEMENTS

The National Radio Astronomy Observatory is a facility of the National Science Foundation operated under cooperative agreement by Associated Universities, Inc. This work was supported by NASA *Fermi* Grant NNX10AD14G and a WV EPSCoR grant.

## REFERENCES

- Abdo, A. A., et al. 2010, *ApJ*, 708, 1254  
 Allen, C. W. 1973, London: University of London, Athlone Press, —c1973, 3rd ed.  
 Argyle, E., & Gower, J. F. R. 1972, *ApJ*, 175, L89  
 Atwood, W. B., et al. 2009, *ApJ*, 697, 1071  
 Bednarek, W., & Idec, W. 2011, *MNRAS*, 414, 2229  
 Bhat, N. D. R., Wayth, R. B., Knight, H. S., et al. 2007, *ApJ*, 665, 618  
 Bhat, N. D. R., Tingay, S. J., & Knight, H. S. 2008, *ApJ*, 676, 1200  
 Bietenholz, M. F., Kassim, N., Frail, D. A., et al. 1997, *ApJ*, 490, 291  
 Bilous, A. V., Kondratiev, V. I., McLaughlin, M. A., Ransom, S. M., Lyutikov, M., Mickaliger, M., & Langston, G. I. 2011, *ApJ*, 728, 110  
 Bykov, A. M., Pavlov, G. G., Artemyev, A. V., & Uvarov, Y. A. 2012, *MNRAS*, 421, L67  
 Cerutti, B., Uzdensky, D. A., & Begelman, M. C. 2012, *ApJ*, 746, 148  
 Collins, S., Shearer, A., Stappers, B., et al. 2012, *IAU Symposium*, 285, 296  
 Cordes, J. M., & McLaughlin, M. A. 2003, *ApJ*, 596, 1142  
 Cordes, J. M., Bhat, N. D. R., Hankins, T. H., McLaughlin, M. A., & Kern, J. 2004, *ApJ*, 612, 375  
 DuPlain, R., Ransom, S., Demorest, P., et al. 2008, *Proc. SPIE*, 7019, 70191D  
 Espinoza, C. M., Jordan, C., Stappers, B. W., Lyne, A. G., Weltevrede, P., Cognard, I., & Theureau, G. 2010, *The Astronomer’s Telegram*, 2889, 1  
 Hays, E., Buehler, R., D’Ammando, F., Grove, J. E., & Ray, P. S. 2010, *The Astronomer’s Telegram*, 2879, 1  
 Hankins, T. H., & Eilek, J. A. 2007, *ApJ*, 670, 693  
 Hotan, A. W., van Straten, W., & Manchester, R. N. 2004, *PASA*, 21, 302  
 Istomin, Y. N. 2004, *Young Neutron Stars and Their Environments*, 218, 369  
 Jessner, A., Popov, M. V., Kondratiev, V. I., et al. 2010, *A&A*, 524, A60  
 Karuppusamy, R., Stappers, B. W., & van Straten, W. 2010, *A&A*, 515, A36  
 Karuppusamy, R., Stappers, B. W., & Lee, K. J. 2012, *A&A*, 538, A7  
 Kramer, M., Johnston, S., & van Straten, W. 2002, *MNRAS*, 334, 523  
 Kuz’min, A. D., Belyatsky, Y. A., Dumsky, D. V., et al. 2011, *Astronomy Reports*, 55, 416  
 Langston, G. 2007, *Highlights of Astronomy*, 14, 367  
 Lorimer, D. R., Yates, J. A., Lyne, A. G., & Gould, D. M. 1995, *MNRAS*, 273, 411  
 Lundgren, S. C. 1994, Ph.D. Thesis, Cornell Univ., Ithaca, NY  
 Lundgren, S. C., Cordes, J. M., Ulmer, M., Matz, S. M., Lomatch, S., Foster, R. S., & Hankins, T. 1995, *ApJ*, 453, 433  
 Lyne, A. G., Pritchard, R. S., & Graham-Smith, F. 1993, *MNRAS*, 265, 1003  
 Lyutikov, M., Blandford, R. D., & Machabeli, G. 1999, *MNRAS*, 305, 338  
 Lyutikov, M. 2007, *MNRAS*, 381, 1190  
 Machabeli, G. Z., & Usov, V. V. 1979, *Soviet Astronomy Letters*, 5, 238  
 Majid, W. A., Naudet, C. J., Lowe, S. T., & Kuiper, T. B. H. 2011, *ApJ*, 741, 53  
 Miller, J. J., et al. in prep.  
 Moffett, D. A., & Hankins, T. H. 1996, *ApJ*, 468, 779  
 Moffett, D. A. 1997, Ph.D. Thesis, New Mexico Inst. Mining and Technology  
 Parsons, A., Werthimer, D., Backer, D., et al. 2009, *astro2010: The Astronomy and Astrophysics Decadal Survey*, 2010, 21

- Petrova, S. A. 2006, Chinese Journal of Astronomy and Astrophysics Supplement, 6, 020000
- Petrova, S. A. 2009, MNRAS, 395, 1723
- Popov, M. V., Soglasnov, V. A., Kondratiev, V. I., Kostyuk, S. V., Ilyasov, Y. P., & Oreshko, V. V. 2006, Astronomy Reports, 50, 55
- Popov, M. V., & Stappers, B. 2007, A&A, 470, 1003
- Popov, M. V., Soglasnov, V. A., Kondratiev, V. I., et al. 2008, Astronomy Reports, 52, 900
- Popov, M., Soglasnov, V., Kondratiev, V., et al. 2009, PASJ, 61, 1197
- Rankin, J. M., Comella, J. M., Craft, H. D., Jr., Richards, D. W., Campbell, D. B., & Counselman, C. C., III 1970, ApJ, 162, 707
- Rickett, B. J., & Lyne, A. G. 1990, MNRAS, 244, 68
- Ritchings, R. T. 1976, MNRAS, 176, 249
- Scargle, J. D. 1982, ApJ, 263, 835
- Serylak, M., et al. 2009, MNRAS, 394, 295
- Shearer, A., Stappers, B., O’Conner, P., Golden, A., Strom, R., Redfern, M., & Ryan, O. 2003, Science, 301, 493
- Smirnova, T. V., & Logvinenko, S. V. 2009, Astronomy Reports, 53, 334
- Staelin, D. H., & Reifenstein, E. C., III 1968, Science, 162, 1481
- Tavani, M., et al. 2011, Science, 331, 736
- Weatherall, J. C. 1998, ApJ, 506, 341
- Zhuravlev, V. I., Popov, M. V., Kondratiev, V. I., et al. 2011, Astronomy Reports, 55, 724

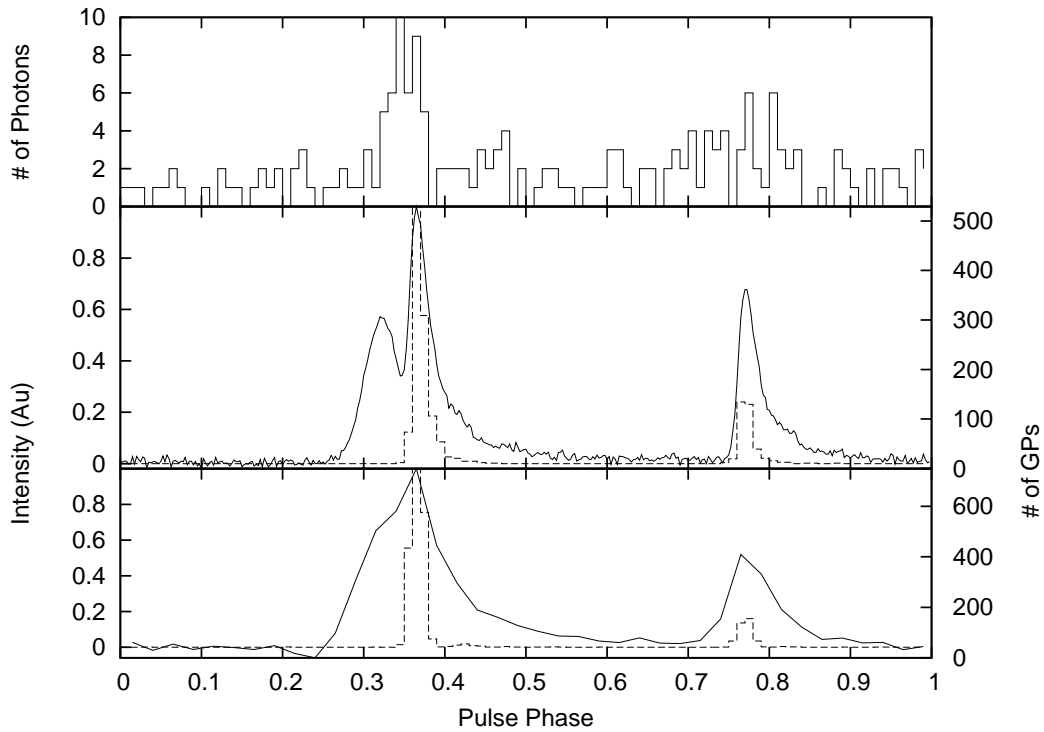


FIG. 1.— Folded pulse profiles from MJD 55406 for *Fermi* (top), the GBT (middle, solid line), and the GB43 (bottom, solid line), as well as histograms of the number of GPs for the GBT (middle, dashed line) and GB43 (bottom, dashed line). The *Fermi* profile is made using photons above 100 MeV over a 24 hour period ( $\sim 11$  hours on source time). The GB43 observations were taken at a center frequency of 330 MHz over a 220 MHz band for 3.7 hours and the GBT observations were taken at a center frequency of 350 MHz over a 100 MHz band for 10 minutes. The folded radio profiles have been normalized to have peaks of unity.

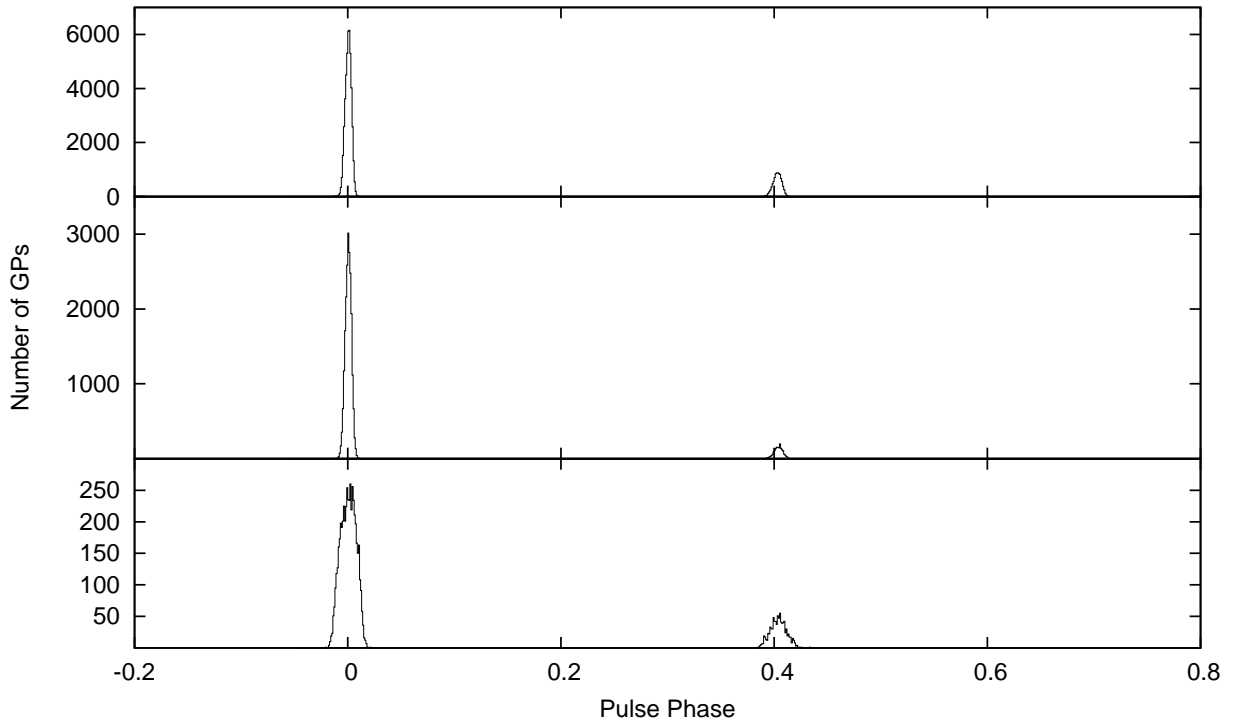


FIG. 2.— Number of GPs versus pulse phase for all GPs collected with the GB43 at 1.2 GHz (top, post-flare; middle, pre-flare) and 330 MHz (bottom). Most GPs at frequencies below 5 GHz come at the phase ( $\sim 0$ ) of the MP, while there are still a considerable number at the IP phase ( $\sim 0.4$ ). No GPs are seen at other phases. The FWHMs of the 1.2 GHz distributions ( $226 \mu\text{s}$  pre-flare,  $292 \mu\text{s}$  post-flare) are on the order of the FWHMs of the folded profiles at 1.2 GHz, while the FWHM of the 330 MHz distribution ( $704 \mu\text{s}$ ) is much narrower than the folded profile and is on the order of the average GP profile at 330 MHz. Even though there were only four observing epochs after the flare, there were many more GPs recorded than pre-flare due to a large increase in receiver sensitivity.

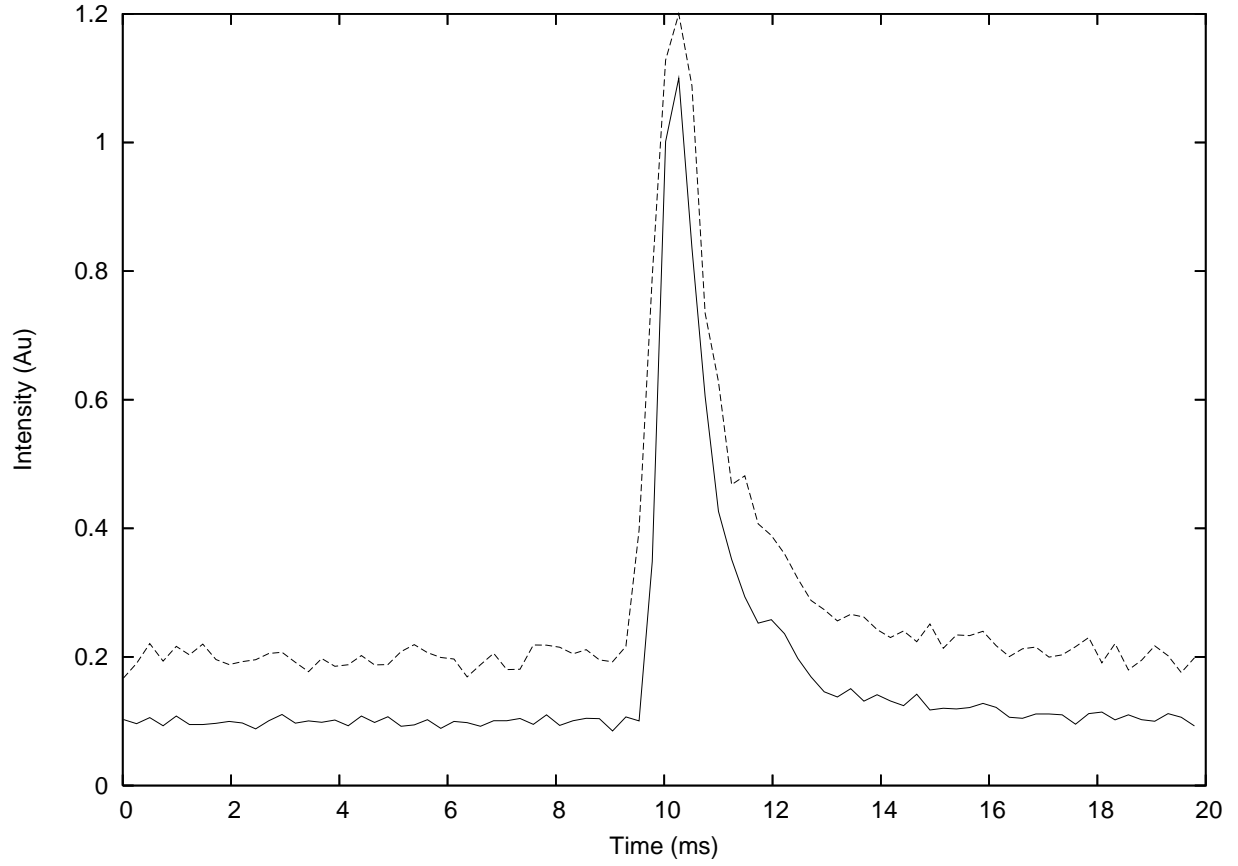


FIG. 3.— A single GP observed both with the GB43 (dashed line) at 330 MHz and the GBT (solid line) at 350 MHz on MJD 55406. When corrected for the dispersion delay due to different observing frequencies, the peaks of the GP from both observations are within one  $\mu\text{s}$  of each other. The GB43 profile has been shifted upwards for clarity.

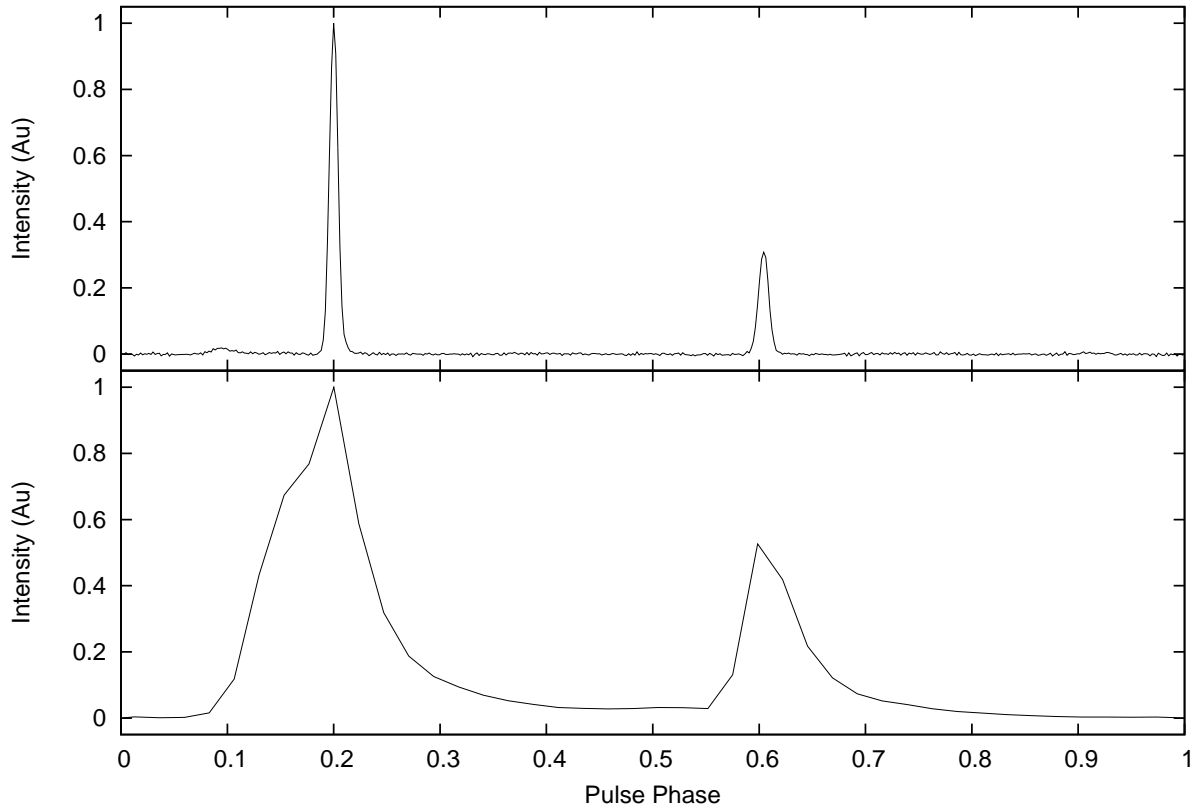


FIG. 4.— Average pulse profiles from all 1.2 GHz (top) and 330 MHz (bottom) observations with the GB43, listed in Table 1. The 1.2 GHz profile excludes MJDs 55097, 55257, 55290, 55299, and 55346, where the folded pulse profiles were dominated by RFI. At 1.2 GHz the MP (larger) and IP (smaller) are apparent, and a low-frequency component can be seen one-tenth of a pulse phase ahead of the MP (e.g. Moffett & Hankins 1996). At 330 MHz the MP and IP are much wider due to large DM smearing, which at the top of the band (440 MHz) is 0.3 ms and at the bottom (220 MHz) is 2.4 ms. The scattering time, estimated from Kuz'min et al. (2011), is  $470 \mu\text{s}$  at the top of the band and 5.8 ms at the bottom, and the sampling time is  $819.2 \mu\text{s}$ . This leads to an effective resolution of  $990 \mu\text{s}$  at the top of the band and 6.3 ms at the bottom.

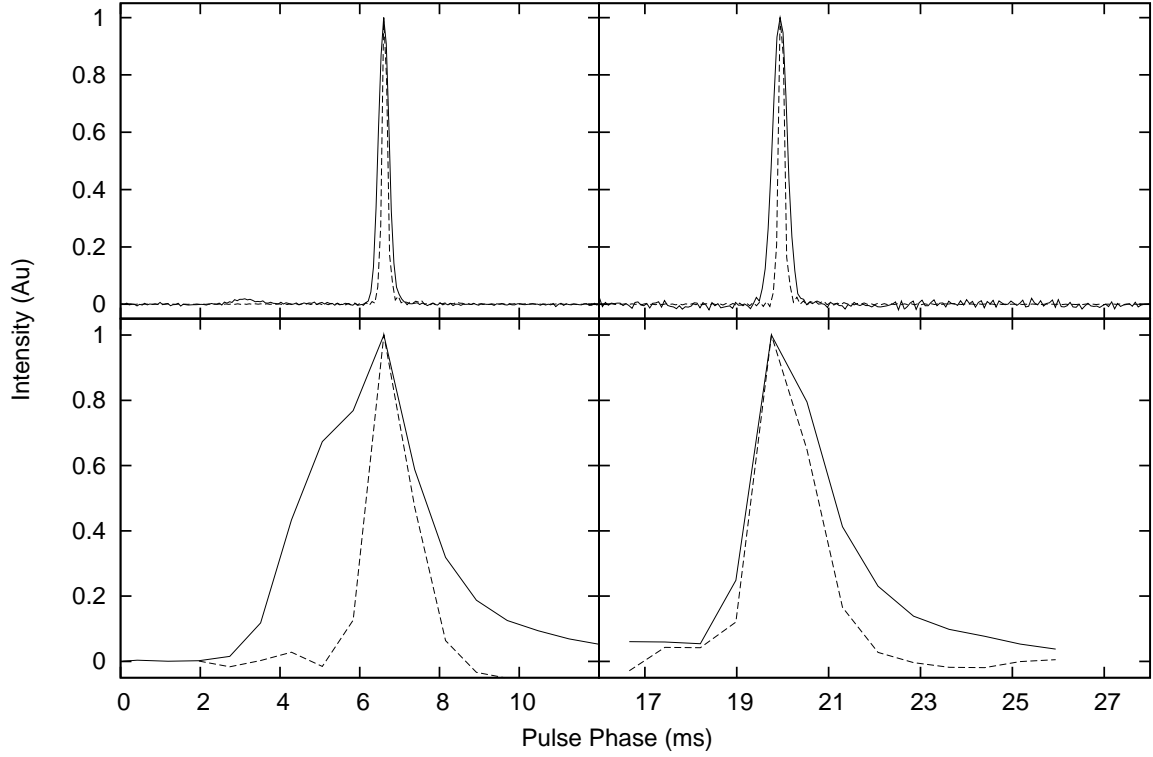


FIG. 5.— Average GP profiles for all MP (left) and IP (right) GPs (dashed lines) collected with the GB43 at 1.2 GHz (top) and 330 MHz (bottom). The 1.2 GHz profiles are made by summing the 76707 individual MP and 10871 individual IP GP profiles, and the 330 MHz profiles are made by summing the 5232 individual MP and 888 individual IP GP profiles. They are shown with the folded MP and IP profiles for all 1.2 GHz and 330 MHz data (solid lines). The FWHM of the 1.2 GHz folded MP and IP are  $\sim 305 \mu\text{s}$  and  $\sim 360 \mu\text{s}$ , respectively, while the FWHM of the average MP and IP GPs are both  $\sim 140 \mu\text{s}$ . The FWHM of the 330 MHz folded MP and IP are  $\sim 3.2 \text{ ms}$  and  $\sim 1.5 \text{ ms}$ , respectively, while the FWHM of the average MP and IP GPs are  $\sim 1.1 \text{ ms}$ . The 330 MHz MP is much wider than the IP due to its overlap with the MP precursor. The intensities of the profiles are arbitrary and are scaled for clarity.

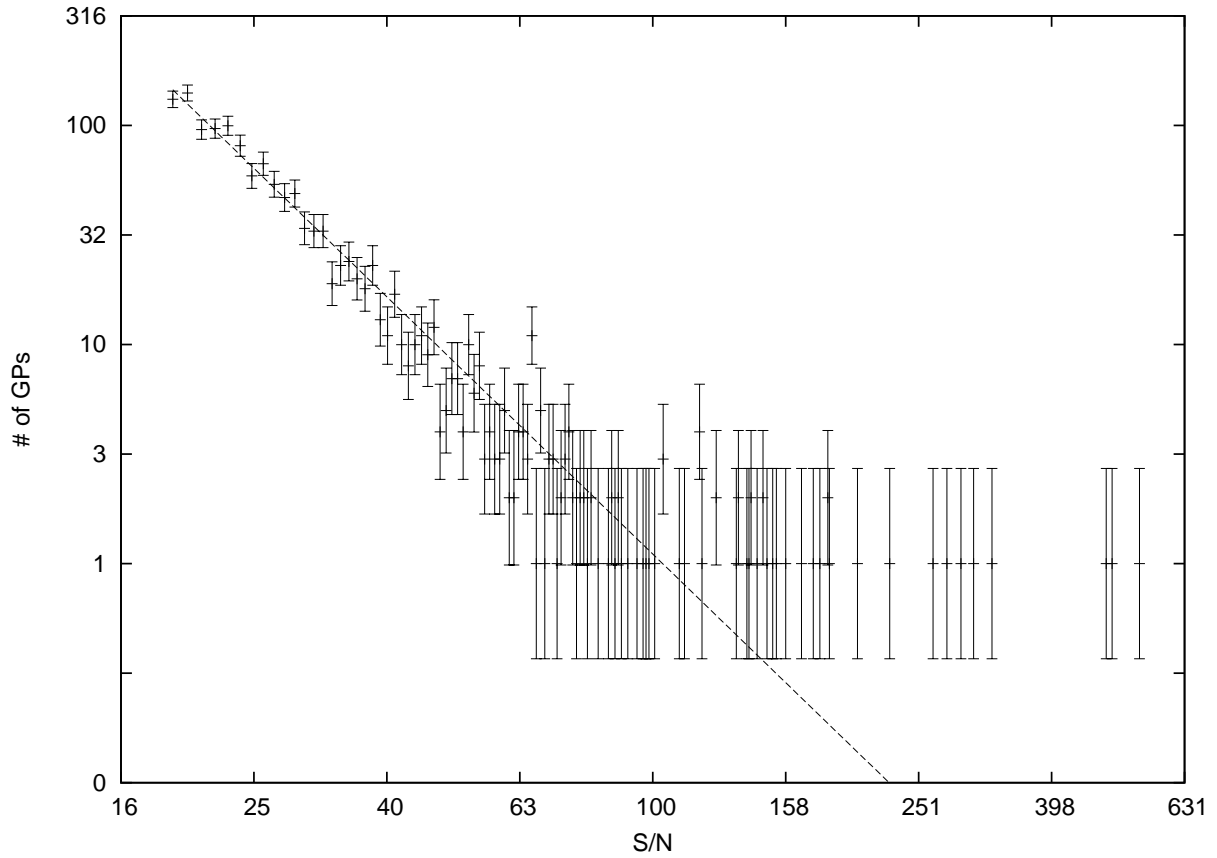


FIG. 6.— A plot of the log of the number of GPs collected with the GB43 vs the log of their S/N for the MP at 1.2 GHz on MJD 55099 and a best-fit power-law, which has a slope of  $2.93 \pm 0.07$ . The deviation from the power-law distribution at high S/N is seen on all days, and these GPs may be examples of supergiant pulses, seen previously by Cordes et al. (2004). The average supergiant pulse is about 15 times stronger than the average GP.

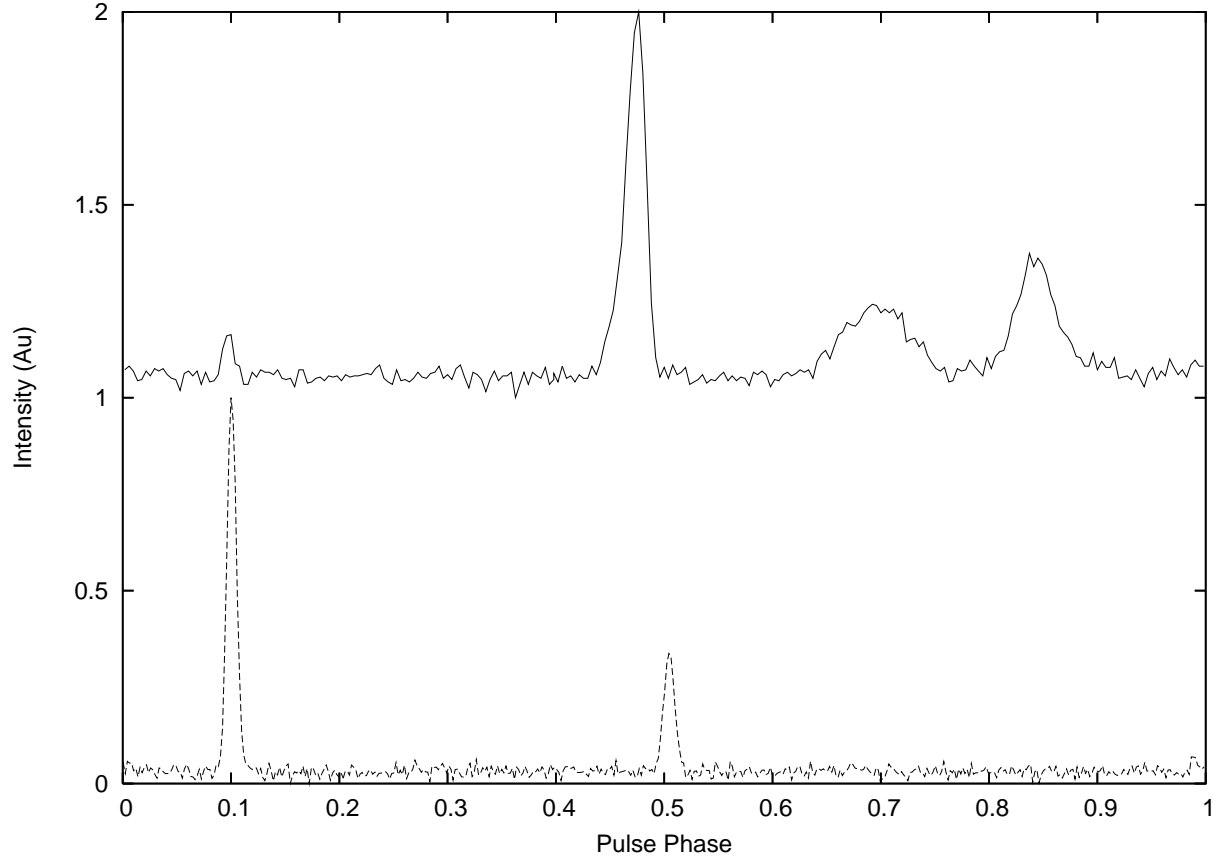


FIG. 7.— Average profiles from the GBT at 8.9 GHz (solid line, from Bilous et al. (2011)) and the GB43 at 1.2 GHz (dashed line). The weakening of the MP at high frequencies can be seen, as well as the strengthening and shift of the IP.

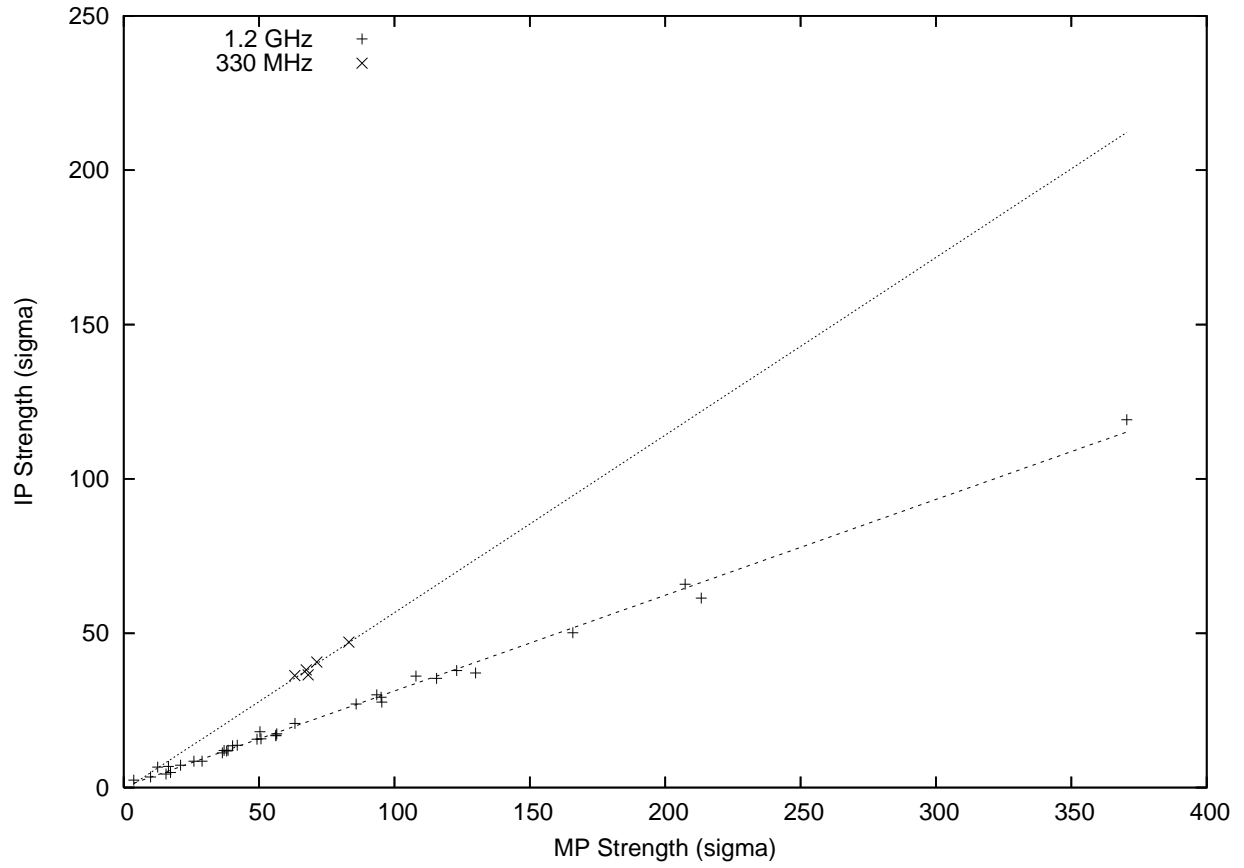


FIG. 8.— Comparison of the strength of the MP of the folded profile to that of the IP for each observation. There is an obvious linear trend in both the 330 MHz and 1.2 GHz data, with slopes of  $0.58 \pm 0.08$  and  $0.310 \pm 0.004$ , respectively. This supports the theory that the IP may be a reflection of the MP off of the magnetosphere.

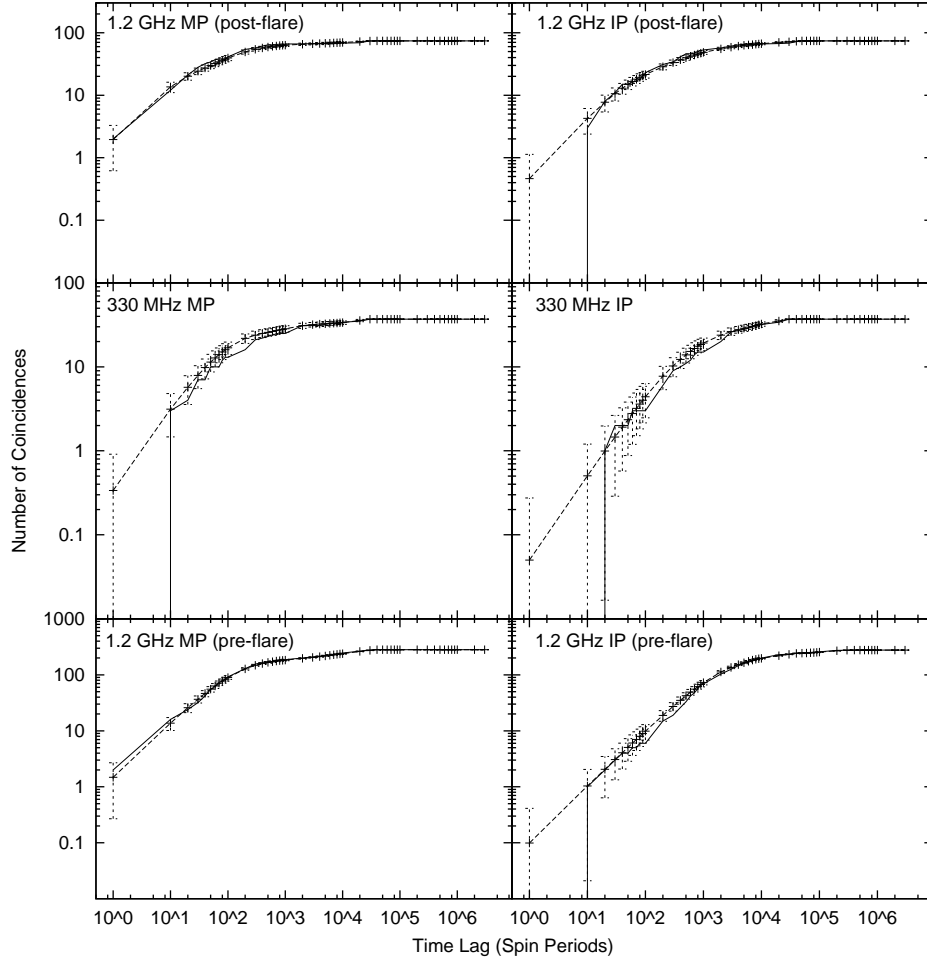


FIG. 9.— Number of coincidences between *Fermi* photons and GB43 GP TOAs (solid lines), as well as the number of coincidences between randomized *Fermi* photons and GP TOAs (dotted line) with  $1\sigma$  error bars. The bottom row is the correlation with the 1.2 GHz pre-flare data, the middle row is the 330 MHz data, and the top row is the 1.2 GHz post-flare data. For each row the MP is the left panel and the IP is the right panel.

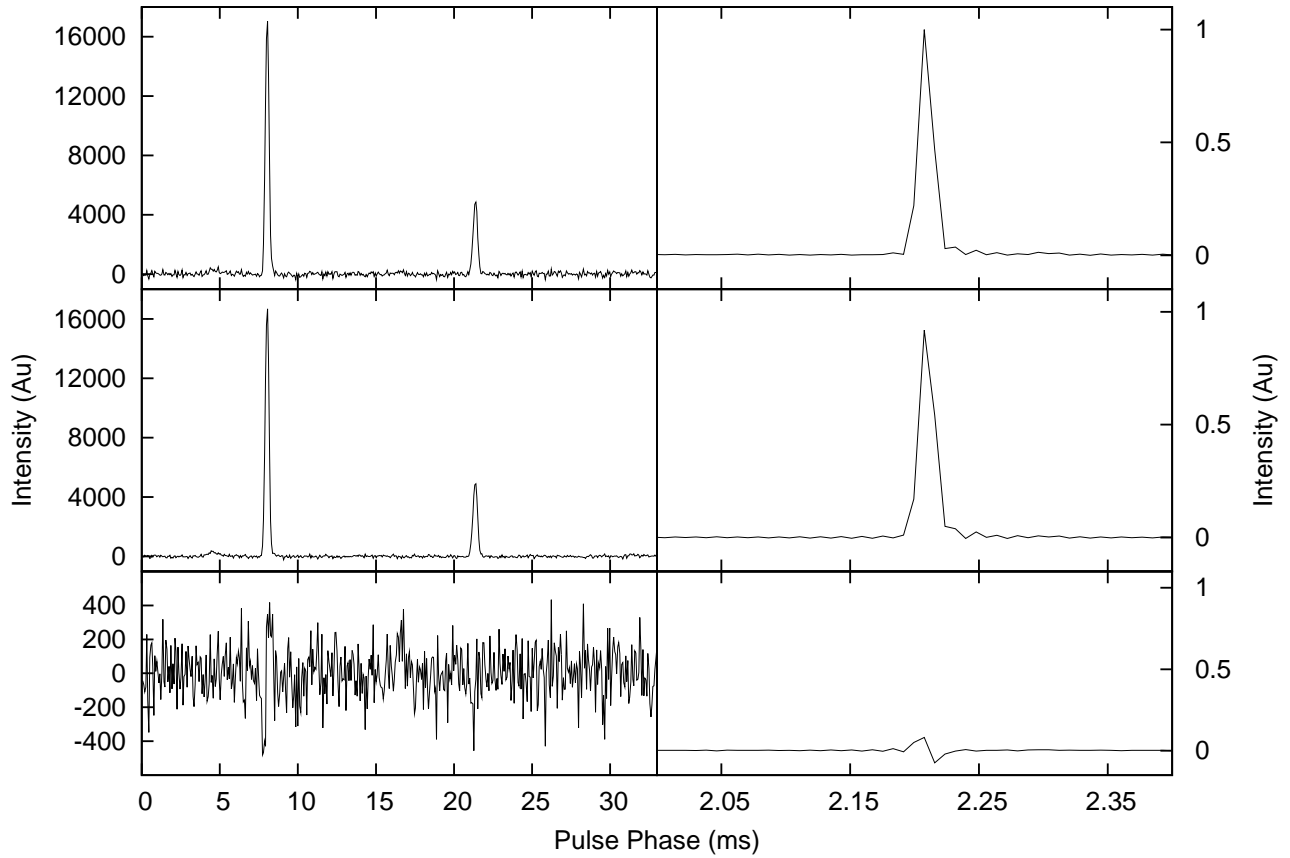


FIG. 10.— A  $\gamma$ -ray flare occurred from MJDs 55457–55461, so we checked for changes in the average pulse shape and GP shape. *Left:* The folded pulse profiles from 1.2 GHz GB43 observations on MJD 55352 (top) and MJD 55532 (middle), and the difference between them (bottom). The profiles are scaled so that the area under the main pulse for both profiles is the same. As can be seen from the bottom plot, the difference is on the order of the rms noise, so there is no statistically significant change in pulse shape. *Right:* The average GP profiles from 1.2 GHz GB43 observations on MJD 55352 (top) and MJD 55532 (middle), and the difference between them (bottom). This difference is not significant as there is a larger variation in average GP shape between pre-flare days. The profiles are also scaled so that the area under the main pulse for both profiles is the same.

TABLE 1

OBSERVATIONAL PARAMETERS INCLUDING THE MJD THE OBSERVATION WAS TAKEN, THE CENTER FREQUENCY USED, THE LENGTH OF THE OBSERVATION, THE SAMPLING TIME, THE DM USED FOR DEDISPERSION, AND THE NUMBER OF GPs FOUND WITH  $S/N \geq 10$ . THE STARRED MJDs ARE DAYS IN WHICH SIMULTANEOUS OBSERVATIONS WITH THE GBT OCCURED.

MJD	Frequency (MHz)	Observation Length (min)	Sampling Time ( $\mu$ s)	DM ( $\text{pc cm}^{-3}$ )	Number of MP GPs	Number of IP GPs
55079	1200	5	204.8	56.8005	33	1
55079	1200	108	204.8	56.8005	341	27
*55083	1200	4	204.8	56.8005	19	1
*55083	1200	120	204.8	56.8005	582	42
55085	1200	120	204.8	56.8005	73	0
*55086	1200	156	204.8	56.8005	1677	96
*55090	1200	150	204.8	56.8005	551	31
*55093	1200	168	204.8	56.8005	650	42
*55095	1200	108	51.2	56.8005	669	47
*55096	1200	150	204.8	56.8005	264	21
*55097	1200	240	204.8	56.8005	519	45
*55099	1200	210	204.8	56.8005	1435	76
*55102	1200	150	204.8	56.8005	1228	76
55118	1200	6	204.8	56.8109	2	0
55118	1200	6	51.2	56.8109	16	0
55139	1200	240	51.2	56.8229	3757	308
55142	1200	120	51.2	56.8229	244	22
55172	1200	22	51.2	56.8279	25	0
55178	1200	282	51.2	56.8279	1808	110
55180	1200	114	51.2	56.8279	478	27
55240	1200	7	245.76	56.8053	32	2
55240	1200	180	122.88	56.8053	1575	101
55256	1200	15	61.44	56.8622	148	8

MJD	Frequency (MHz)	Observation Length (min)	Sampling Time ( $\mu$ s)	DM ( $\text{pc cm}^{-3}$ )	Number of MP GPs	Number of IP GPs
55257	1200	198	245.76	56.8622	1098	76
55261	1200	492	245.76	56.8622	41	9
55264	1200	15	61.44	56.8622	106	5
55269	1200	360	245.76	56.8622	42	2
55270	1200	30	245.76	56.8622	291	17
55284	1200	180	245.76	56.8622	1094	63
55290	1200	108	245.76	56.8228	169	10
55299	1200	10	245.76	56.8228	4	0
55304	1200	60	245.76	56.8228	73	5
55346	1200	60	245.76	56.8022	672	40
55347	1200	120	245.76	56.8022	1170	76
55347	1200	168	61.44	56.8022	2701	243
55352	1200	240	61.44	56.8022	2182	146
55403	330	37	223.42	56.7988	271	31
55405	330	60	819.2	56.7988	1201	250
55406	330	222	819.2	56.7988	1775	273
55411	330	60	819.2	56.7962	1332	220
55412	330	30	819.2	56.7962	653	114
55516	1200	550	245.76	56.8065	4870	326
55532	1200	315	61.44	56.7964	11671	937
55539	1200	10	61.44	56.7964	786	146
55541	1200	335	61.44	56.7964	33611	7687

TABLE 2

SAMPLING TIMES, DM SMEARING TIMES, SCATTERING TIMES, AND EFFECTIVE RESOLUTION AT THE TOP AND BOTTOM OF THE BAND FOR THE GB43 330 MHz AND 1.2 GHz OBSERVATIONS, AS WELL AS FOR THE GBT 350 MHz OBSERVATION. THE DM SMEARING TIMES WERE CALCULATED USING THE DELAY BETWEEN TWO CONSECUTIVE CHANNELS CAUSED BY DISPERSION, AND THE SCATTERING TIMES WERE ESTIMATED FROM KUZ'MIN ET AL. (2011). THE SAMPLING TIME LISTED FOR THE 1.2 GHz GB43 OBSERVATION WAS THE MOST COMMON SAMPLING TIME FROM TABLE 1.

Frequency (MHz)	Sampling Time ( $\mu$ s)	DM Smearing Time		Scattering Time		Effective Resolution	
		Top	Bottom	Top	Bottom	Top	Bottom
330 (GB43)	819.2	300 $\mu$ s	2.4 ms	470 $\mu$ s	5.8 ms	990 $\mu$ s	6.3 ms
350 (GBT)	81.92	361 $\mu$ s	855 $\mu$ s	670 $\mu$ s	1.9 ms	765 $\mu$ s	2.0 ms
1200 (GB43)	204.8	23 $\mu$ s	180 $\mu$ s	4 $\mu$ s	54 $\mu$ s	206 $\mu$ s	278 $\mu$ s

TABLE 3

DIFFERENTIAL POWER-LAW MEASUREMENTS FOR THE MP AND IP FOR EACH OBSERVING EPOCH. SOME MJDS HAVE TWO ENTRIES LISTED BECAUSE THERE WERE TWO SEPARATE OBSERVATIONS ON THOSE DAYS. AN X MEANS THAT THERE WERE NOT ENOUGH PULSES RECORDED FOR THE MP OR IP ON THAT DAY TO FIT A POWER-LAW TO THE AMPLITUDE DISTRIBUTION.

MJD	Differential Power-law Index (MP)	Differential Power-law Index (IP)
55079	X	X
55079	2.1±0.3	X
55083	X	X
55083	3.1±0.2	X
55085	X	X
55086	2.70±0.06	X
55090	2.8±0.1	X
55093	2.6±0.2	X
55095	2.9±0.2	X
55096	X	X
55097	X	X
55099	2.93±0.07	X
55102	2.92±0.08	X
55118	X	X
55118	X	X
55139	2.61±0.08	X
55142	X	X
55172	X	X
55178	2.81±0.08	X
55180	X	X
55240	X	X
55240	2.1±0.1	X
55256	X	X

MJD	Differential Power-law Index (MP)	Differential Power-law Index (IP)
55257	$2.1 \pm 0.1$	X
55261	X	X
55264	X	X
55269	X	X
55270	X	X
55284	$2.1 \pm 0.1$	X
55290	X	X
55299	X	X
55304	X	X
55346	$2.4 \pm 0.2$	X
55347	$2.8 \pm 0.1$	X
55347	$2.40 \pm 0.07$	X
55352	$2.21 \pm 0.07$	X
55403	$2.5 \pm 0.2$	X
55405	$2.95 \pm 0.09$	$2.4 \pm 0.2$
55406	$2.94 \pm 0.05$	$3.1 \pm 0.2$
55411	$2.8 \pm 0.1$	$2.9 \pm 0.2$
55412	$2.7 \pm 0.2$	X
55516	$2.93 \pm 0.05$	$2.4 \pm 0.4$
55532	$2.56 \pm 0.05$	$2.7 \pm 0.2$
55541	$2.8 \pm 0.1$	$2.81 \pm 0.03$

TABLE 4  
 COMPARISON OF DIFFERENTIAL POWER-LAW INDICES FOR THE MP AND IP AT BOTH 1.2 GHz AND 330 MHz BETWEEN THIS WORK AND PREVIOUSLY PUBLISHED VALUES.

Frequency (MHz)	Differential Power-law Index (MP)	Differential Power-law Index (IP)	Reference
112	3.3 <sup>a</sup>	–	Smirnova & Logvinenko (2009)
146	3.5	3.8	Argyle & Gower (1972)
200	2.7 <sup>a</sup>	–	Bhat et al. (2007)
330	2.5–3.0	2.4–3.1	This work
430	2.3	– <sup>b</sup>	Cordes et al. (2004)
600	3.2	3.0	Popov et al. (2009)
812	3.3 <sup>a</sup>	–	Lundgren et al. (1995)
1200	2.7–4.2	2.6	Popov & Stappers (2007)
1200	2.1–3.1	2.4–2.8	This work
1300	2.3 <sup>a</sup>	–	Bhat et al. (2008)
1400	2.8	3.1	Karuppusamy et al. (2010)
2100	3.0 <sup>a</sup>	–	Zhuravlev et al. (2011)
4850	2.8 <sup>a</sup>	–	Popov et al. (2008)

<sup>a</sup> MP and IP GPs were combined in these analyses

<sup>b</sup> No measurement was taken for the IP

TABLE 5  
 DIFFERENTIAL POWER-LAW INDICES FOR DIFFERENT SOURCE CLASSES FOR COMPARISON WITH GP POWER-LAWS.

Source Class	Power-law Index	Reference
Normal Pulsars	3.85	Kramer et al. (2002)
Magnetars	2.1–7.7	Serylak et al. (2009)
RRATs	3.0	Miller et al. (in prep.)

TABLE 6  
 MAXIMUM CORRELATION/ANTICORRELATION FOR EACH FREQUENCY AT EACH ENERGY CUT, AND THE TIME LAGS AT WHICH THEY OCCUR. NOTE THAT THE MAXIMUM CORRELATION FOR THE 330 MHz IP WITH THE 500 MeV ENERGY CUT IS NEGATIVE.

Energy Cut	Frequency (MHz)	MP/IP	Max Correlation ( $\sigma$ )	Time Lag (Spin Periods)	Max Anti-correlation ( $\sigma$ )	Time Lag (Spin Periods)
100 MeV	Pre-flare 1200	MP	+1.4	30000	-0.9	30
		IP	+2.1	200000	-1.7	300
	330	MP	+0.2	10000	-2.1	200
		IP	+0.5	30	-1.5	1000
	Post-flare 1200	MP	+1.5	40	-2.4	20000
		IP	+1.9	500	-2.3	30000
500 MeV	Pre-flare 1200	MP	+2.3	1	-0.4	8000
		IP	+1.5	20000	-1.5	700
	330	MP	+0.1	6000	-1.7	200
		IP	-0.1	300	-1.7	2000
	Post-flare 1200	MP	+0.8	200	-3.5	20000
		IP	+1.0	200	-2.7	30000
1 GeV	Pre-flare 1200	MP	+3.2	1	-0.1	60
		IP	+2.0	5000	-1.2	200
	330	MP	+0.8	6000	-0.9	10
		IP	+0.9	6000	-1.1	100
	Post-flare 1200	MP	+1.9	60	-0.4	1
		IP	+2.1	3000	-0.7	10